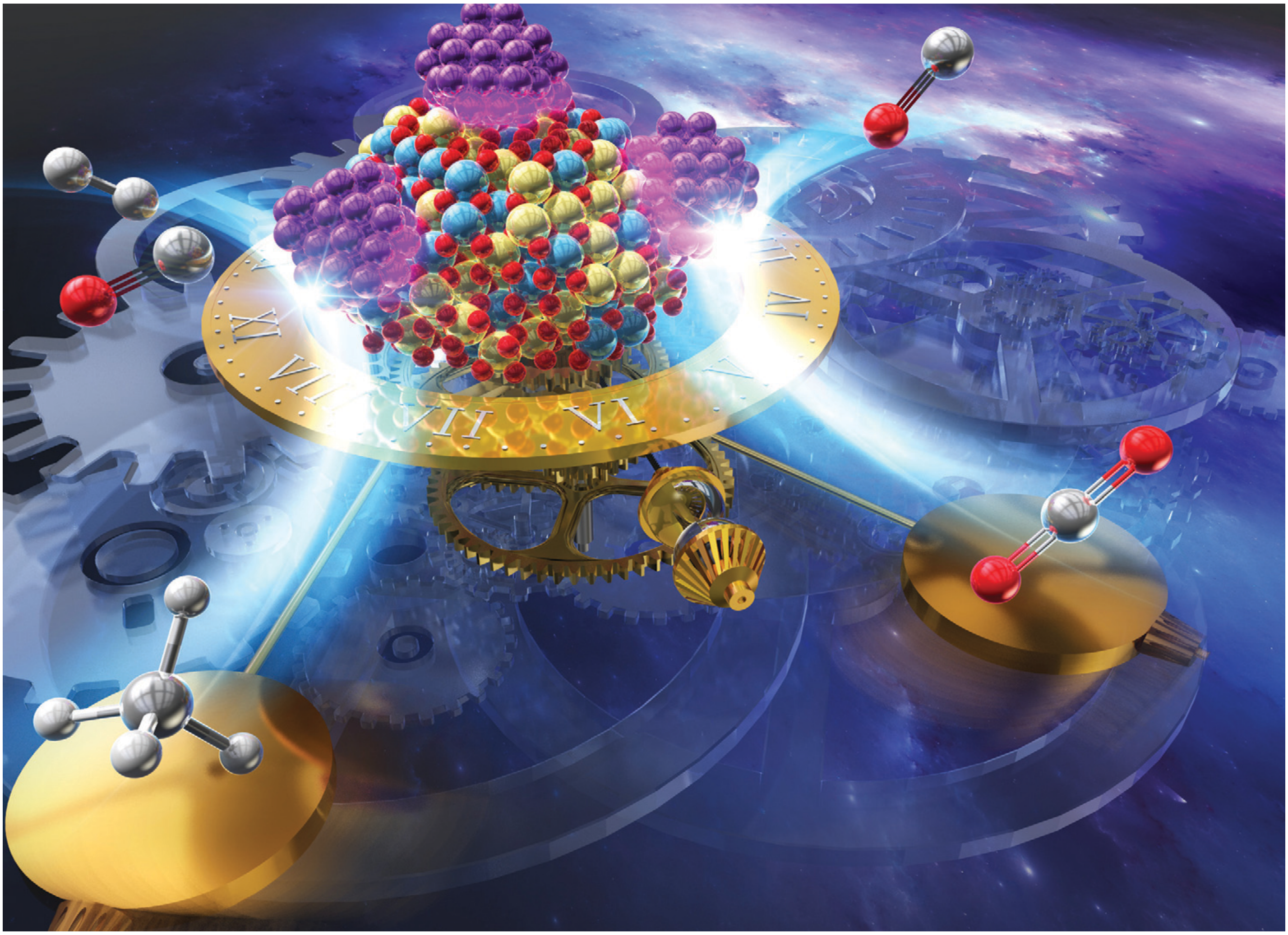

Showcasing research from Professor Sekine's laboratory, Department of Applied Chemistry, Waseda University, Tokyo, Japan.

Low-temperature catalytic chemical looping dry reforming of methane over Ru/$La_2Ce_2O_7$

The chemical looping method was applied to the reaction of methane and carbon dioxide, and the Ru/$La_2Ce_2O_7$ catalyst + oxygen carrier showed high and stable activity for long cycles, even at low temperatures.

As featured in:

Catalysis Science & Technology

See Yasushi Sekine *et al.*, *Catal. Sci. Technol.*, 2024, **14**, 3609.

ROYAL SOCIETY OF **CHEMISTRY**

rsc.li/catalysis

Catalysis
Science &
Technology

ROYAL SOCIETY
OF CHEMISTRY

PAPER

View Article Online
View Journal | View Issue

Cite this: *Catal. Sci. Technol.*, 2024, **14**, 3609

Low-temperature catalytic chemical looping dry reforming of methane over Ru/$La_2Ce_2O_7$†

Keke Kang, Naoki Kayama, Takuma Higo,
Clarence Sampson and Yasushi Sekine *

Chemical looping dry reforming of CH_4, a promising approach to reduce fossil fuel consumption and use CO_2, hinges on designing an efficient oxygen carrier. However, high operating temperatures and unsatisfactory performance hamper its application. Loading a small amount of Ru promoter on the $La_2Ce_2O_7$ oxygen carrier enhances CH_4 activation considerably, lowering the onset temperature to around 545 K. The Ru/$La_2Ce_2O_7$ material exhibited impressive performance, achieving CH_4 conversion of around 65%, with almost negligible CO_2 produced during the reduction step and CO_2 conversion exceeding 95% during the CO_2 re-oxidation step over 10 redox cycles. Despite slight carbon deposition, the redox performance remains stable because of efficient carbon removal in the reoxidation step and the inherent structure stability of the oxygen carrier. This superior performance is attributed to the strong metal–support interaction between Ru and $La_2Ce_2O_7$, forming Ru–O–Ce bonds at the $Ru^{\delta+}$–CeO_{2-x} interface. These bonds anchor active Ru onto stable $La_2Ce_2O_7$ with excellent oxygen-ionic conductivity, enhancing CH_4 activation by increasing surface oxygen vacancies and maintaining structural stability with well-dispersed Ru promoters during cycles. Moreover, the migration of O^{2-} in subsurface is promoted by creating an elevated oxygen chemical potential gradient induced by the oxygen-deprived surface, facilitated by the Ru promoter.

Received 7th April 2024,
Accepted 16th May 2024

DOI: 10.1039/d4cy00450g

rsc.li/catalysis

Introduction

Methane (CH_4) and carbon dioxide (CO_2) are significant contributors to Earth's greenhouse effect. CH_4 resources are abundant and are readily accessible from the exploitation of shale gas or biogas. Therefore, converting CH_4 and CO_2 into other value-added chemicals, such as liquid fuels and hydrocarbons, has become a strategic focus worldwide.[1,2] Dry reforming of methane (DRM; eqn (1)), which simultaneously converts the main greenhouse gases of CH_4 and CO_2, enables the production of a synthesis gas (syngas) of H_2 and CO. Diverse valuable chemical hydrocarbons, methanol, and acetic acid are producible *via* different processes using syngas.[2] Nevertheless, DRM entails challenges from high operation temperatures attributable to its endothermic nature. Additionally, it provides only diminished selectivity because of the side reaction of reverse water gas shift (RWGS; eqn (2)) and subsequent deactivation resulting from carbon deposition during CH_4 pyrolysis (eqn (3)) and the Boudouard reaction (eqn (4)).[1,3]

$$CH_4 + CO_2 \rightarrow 2CO + 2H_2 \quad \Delta_r H^\theta(298\ \mathrm{K}) = 260.5\ \mathrm{kJ\ mol^{-1}} \tag{1}$$

$$CO_2 + 4H_2 \rightarrow CH_4 + 2H_2O \quad \Delta_r H^\theta(298\ \mathrm{K}) = -165.0\ \mathrm{kJ\ mol^{-1}} \tag{2}$$

$$CH_4 \rightarrow C + 2H_2 \quad \Delta_r H^\theta(298\ \mathrm{K}) = -74.1\ \mathrm{kJ\ mol^{-1}} \tag{3}$$

$$2CO \rightarrow CO_2 + C \quad \Delta_r H^\theta(298\ \mathrm{K}) = -172.5\ \mathrm{kJ\ mol^{-1}} \tag{4}$$

Catalytic chemical looping (CL) is a promising method for improving conventional DRM. As presented in Fig. 1, DRM–CL can be accomplished using metal oxides (MO_x) acting as oxygen carriers, which gives out lattice oxygen continuously during the reduction step *via* partial oxidation of CH_4 reaction (POM; eqn (5)) and the lattice oxygen vacancy is refilled during the reoxidation step *via* CO_2 splitting reaction (CS; eqn (6)).

$$\mathrm{POM:}\ MO_x + \delta CH_4 \rightarrow MO_{x-\delta} + \delta CO + 2\delta H_2 \tag{5}$$

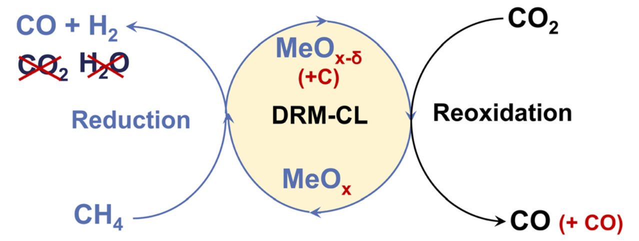

Fig. 1 Schematic image of DRM–CL process.

Applied Chemistry, Waseda University, 3-4-1, Okubo, Shinjuku, Tokyo, Japan. E-mail: ysekine@waseda.jp

† Electronic supplementary information (ESI) available. See DOI: https://doi.org/10.1039/d4cy00450g

$$\text{CO}_2 \text{ splitting: } MO_{x-\delta} + \delta CO_2 \rightarrow MO_x + \delta CO \quad (6)$$

This process remains consistent with the catalytic DRM as a total, even though it involves two distinct gas–solid reactions. Although the overall process would still exhibit its inherent endothermic nature, using chemical looping presents several benefits that are not available when using conventional DRM. First, deactivation by carbon deposition is mitigated because the deposited carbon can be converted by CO_2 *via* the reverse Boudouard reaction (eqn (4)), yielding additional CO during the oxidation step. Moreover, the RWGS side reaction is averted because the produced H_2 is inherently separated from CO_2. Furthermore, the operational conditions can be individually optimised, leading to enhanced performance in specific instances because of the decoupling of reactions.

Selecting suitable oxygen carriers plays a crucially role in the DRM–CL process. However, this approach still presents several difficulties that must be addressed. First, syngas selectivity is diminished because of the presence of CO_2 or H_2O resulting from the total oxidation of methane (eqn (7)). Second, earlier-reported oxygen carriers require high operating temperatures (>1073 K), presenting an obstacle to their integration with downstream low-temperature processes such as Fischer–Tropsch (F–T) synthesis.[4] This limitation also hinders using various cost-effective industrial materials (*e.g.*, stainless steel and so on) with lower melting points or recycled industrial waste heat.[5]

$$\text{Total oxidation of methane: } CH_4 + MO_x \rightarrow CO_2 + H_2O + MO_{x-\delta} \quad (7)$$

$$\text{Methane pyrolysis: } CH_4(+M) \rightarrow 2H_2 + C_{(s)}(+M) \quad (8)$$

The primary hindrance to the reactivity in POM, particularly at lower temperatures, is the great amount of activation energy needed for lattice oxygen migration and removal. Furthermore, syngas selectivity is contingent on the type and abundance of surface oxygen species. Syngas selectivity is also influenced by the relative rates of bulk and subsurface oxygen conduction and surface oxygen reaction during the redox reactions. Moreover, the conduction of bulk and subsurface lattice oxygen to the oxide surface imposes limitations on the overall redox conversion.[6–8] Ce-based materials are highly appealing in DRM–CL because of their oxygen mobility and storage capacity.[9–12] From a thermodynamic perspective, the oxidation of reduced ceria by CO_2 is favourable across a wide temperature range, from 298 K to over 1273 K.[13] Additionally, reduction from CeO_2 to Ce_6O_{11} has been observed by Otsuka *et al.*[14] as occurring at temperatures as low as 923 K, which is consistent with thermodynamic calculations. Doping metals into CeO_2 is an effective strategy for enhancing the reduction of Ce^{4+} to Ce^{3+}.[15,16] Reportedly, $La_2Ce_2O_7$ (denoted LCO) prepared by introducing lanthanum (La) into CeO_2 can create a synergistic effect, leading to high stability and high oxygen-ionic conductivity.[17–20] Furthermore, Ru metal is selected as the promoter because it is highly effective for methane activation, with high selectivity towards syngas, as reported in conventional DRM. It is also less expensive than other noble metals.[21,22] Therefore, we propose an investigation of the performance and properties of Ru/LCO as oxygen carriers for DRM–CL reaction.

As demonstrated by this study, loading small amounts of Ru (0.5 or 1 wt%) to LCO oxygen carrier can activate CH_4 even at a low temperature of approximately 545 K. The 1 wt% Ru/$La_2Ce_2O_7$ material exhibits remarkable performance, achieving CH_4 conversion around 65%, with minimal CO_2 produced during the reduction step and CO_2 conversion exceeding 95% during the re-oxidation step at 923 K over 10 redox cycles. Despite a slight occurrence of carbon deposition during the reduction step, the redox performance remains stable over many cycles because of the efficient conversion of deposited carbon during the oxidation step and the inherent stability of the oxygen carriers. This improvement enables the broader application of DRM–CL, leading to considerable energy and cost savings. The exceptional performance is attributed to forming strong metal–support interaction (SMSI) between Ru and LCO, forming Ru–O–Ce bonds at the $Ru^{\delta+}$–CeO_{2-x} interface. This interaction anchors active Ru components onto stable LCO with excellent ionic conductivity, enhancing methane activation by reducing the energy barrier through increased surface oxygen vacancies and maintaining structural stability with highly dispersed Ru promoters during many cycles. Moreover, the migration of O^{2-} in subsurface is promoted by creating an elevated oxygen chemical potential gradient induced by the oxygen-deprived surface facilitated by the Ru promoter.

Results and discussion

Screening of *x*Ru/LCO catalysis-oxygen carrier

Fig. 2 shows the effect of the loading amount of Ru promoter on the redox performance of *x*Ru/LCO as investigated using CH_4-TPR and isothermal redox experiments. Fig. 2A shows that only a small amount of Ru promoter can improve the CH_4 activation ability of LCO efficiently, presenting lower CH_4 activation onset temperatures at around 545 K. Furthermore, LCO exhibits a lower CH_4 activation onset temperature of 731 K than that of CeO_2, with an almost

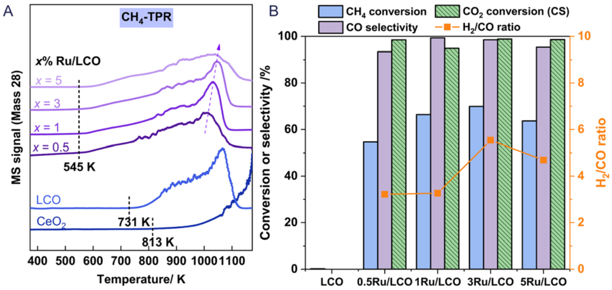

Fig. 2 (A) CH_4-TPR of *x*Ru/LCO and CeO_2; (B) CH_4 conversion, CO selectivity during the reduction step and CO_2 conversion during the reoxidation step of *x*Ru/LCO at 923 K.

complete CO peak at around 1173 K, but no complete peak for CeO_2 even at temperatures higher than 1273 K, which indicates that the doping of La improves the CH_4 activation ability of CeO_2. Moreover, a lower loading amount of Ru promoter results in a lower temperature for the peak amount for CO production, indicating that low loading amounts as 0.5 or 1 wt% Ru promoter are able to activate CH_4 toward syngas with superior performance. Therefore, *x*Ru/LCO exhibits promise for DRM–CL because of its capability to generate substantial oxygen vacancies at low temperatures (*ca.* 545 K) through reaction with CH_4.

Regarding performance during the reduction step at 923 K in Fig. 2B, all Ru-promoted samples exhibit CO selectivity exceeding 95% and CH_4 conversion surpassing 50%. However, the performance results show that LCO remains almost inert for CH_4 at 923 K without Ru promoter, highlighting the key role of Ru on CH_4 activation. Most notably, CH_4 conversion shows a volcanic shape with a maximum value of 70% when the loading amount is 3 wt%. The carbon deposition characterised by H_2/CO ratio also shows a volcanic shape with the most severe carbon deposition ($H_2/CO = 5.5$) occurring when the loading amount is 3 wt%. A possible reason for these results is the following: When the loading amount of Ru promoter is less than 3 wt%, the CH_4 activation is enhanced with the increased amount of Ru promoter. However, as shown in Table S1,† a loading amount of Ru promoter that is greater than 3 wt% leads to a larger mean particle size (obtained by XRD) and a smaller surface area (obtained by BET). Consequently, the active Ru promoters cannot be fully exposed to the oxygen carrier surface to activate CH_4. Regarding performance in the CO_2 reoxidation step, nearly 100% CO_2 conversion was achieved for all Ru-promoted samples. Above all, the findings indicate that satisfactory conversion and high selectivity can be attained at 923 K using very low-load Ru (0.5 or 1 wt%). Furthermore, considering the detection limit of characterisation instruments, 1Ru/LCO instead of 0.5Ru/LCO should be selected for additional study to obtain more precise surface characterisation results, although $x = 0.5$ already shows satisfactory performance results at 923 K.

Redox performance of 1Ru/LCO at different temperatures

Fig. 3A shows the redox performance of 1Ru/LCO during isothermal DRM–CL at various temperatures. 1Ru/LCO exhibits methane conversion of 16% at temperatures as low as 773 K, and it reaches almost 100% when temperatures rise to 1073 K. Regarding the carbon deposition characterised by H_2/CO ratio, it decreases as temperatures rise at temperatures lower than 923 K, but it reaches a stable value of approximately 3 at 923–1073 K. Although it is higher than the ideal value of 2, indicating the appearance of carbon deposition, it was verified later that all the carbon produced can be converted into additional CO *via* the reverse Boudouard reaction during the CO_2 reoxidation step, resulting in zero net coke formation during DRM–CL.

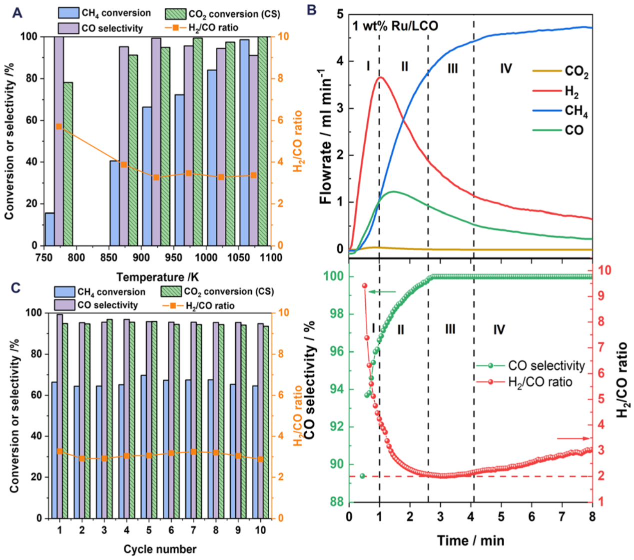

Fig. 3 (A) Comparison of the CH_4 conversion, CO selectivity, CO_2 conversion (CS reaction in the oxidation step) and H_2/CO ratio of 1Ru/LCO at different temperatures. (B) The evolved gas composition in the reduction step over 1Ru/LCO at 923 K: total methane oxidation region (region I), transition region (region II), partial methane oxidation region (region III); methane decomposition region (region IV). (C) Average CH_4 conversion and CO selectivity as well as H_2/CO ratio in the reduction step and CO_2 conversion in the oxidation step during 10 successive redox cycles over 1Ru/LCO at 923 K.

Furthermore, 1Ru/LCO shows CO selectivity higher than 90% within 773–1073 K, indicating a highly selective surface for the production of CO instead of CO_2. Moreover, excellent CO_2 conversion of 78% at temperatures as low as 773 K and conversion approaching 100% over 973 K is obtained on 1Ru/LCO during the CO_2 reoxidation step. Above all, based on a comprehensive consideration of the temperature, conversion rate and selectivity, a standard operation temperature of 923 K should be selected for the following isothermal redox performance evaluations.

Kinetic profiles

Fig. 3B shows that profiles of H_2 concentrations increase remarkably followed a little later by CO concentrations, with negligible CO_2 produced when CH_4 is introduced. According to the corresponding calculated H_2/CO ratio and CO selectivity, the reaction progress is divisible into four consecutive regions according to the H_2/CO ratio and CO selectivity. During the initial period (region I), the remaining active surface oxygen species after H_2 pretreatment leads to total methane oxidation reaction and good catalytic performance of Ru metal for methane decomposition causing the carbon deposition. After gradual consumption of the surface oxygen species, the subsurface oxygen species can partially oxidise methane to CO and H_2 (region III). A transition region (region II) is predominant between region I and region III. When oxygen species are consumed further, the region of carbon formation dominates by methane decomposition (region IV). Therefore, the carbon deposition can be alleviated efficiently by controlling the reaction time of the reduction step with CH_4.

Stability test

The long-term stability of 1Ru/LCO was studied by gas phase detection in the successive 10 redox cycles at 923 K, as portrayed in Fig. 3C. The 1Ru/LCO sample shows high CH_4 conversion around 65% with almost no CO_2 produced in the reduction step and CO_2 conversion exceeding 95% for CS reaction in the reoxidation step at 923 K over 10 redox cycles. Although the H_2/CO ratio remains at around 3, the redox performance remains stable over cycles, demonstrating that the deposited carbon can be well converted during the oxidation step, indicating that the oxygen carrier is well regenerated, and showing that the structure remains stable over many cycles, as confirmed later from XRD and STEM findings. As shown in Fig. S2,† the CO yield in the CS reaction is twice that of the POM reaction. Therefore, the final H_2/CO ratio can be adjusted easily to different values as necessary using the CO produced in the reoxidation step.

To elucidate the state of carbon deposition during redox cycles, 10 redox cycle tests were also conducted using a thermal gravimetric analyser (TGA) by detecting the solid phase for visually observing the weight change caused by the change of carbon deposition. As presented in Fig. 4A, when flowing in CH_4, the weight of the oxygen carrier promptly decreases because of the migration of the lattice oxygen for the POM reaction. Then it increases slowly because of carbon deposition. Afterwards, when flowing in CO_2, it drastically increases to the maximum, first because of the refilling of lattice oxygen. Thereafter, it starts to decrease because of the consumption of the carbon deposited (marked in green) during the reoxidation step. The redox amount of lattice oxygen and the decrease carbon weight during each cycle are calculated and presented in Fig. 4B. A large weight of consumed carbon and a higher oxidation amount than the reduction amount, were observed in cycle 1. After that, the consumed carbon weight during the oxidation step generally decreases along with the number of cycles before being stabilised from cycle 6, because 10 min oxidation by CO_2 is insufficient to remove the high carbon amount completely from cycle 1, leading to carbon accumulation, which is removed with cycles and stabilised because of the lesser amounts of produced carbon during cycles after cycle 1. Accordingly, the redox amount stabilises from cycle 5 with the removal of accumulated carbon from the first cycles, indicating that good stability of 1Ru/LCO is obtainable even with a longer reaction time because of the successful removal of carbon by CO_2.

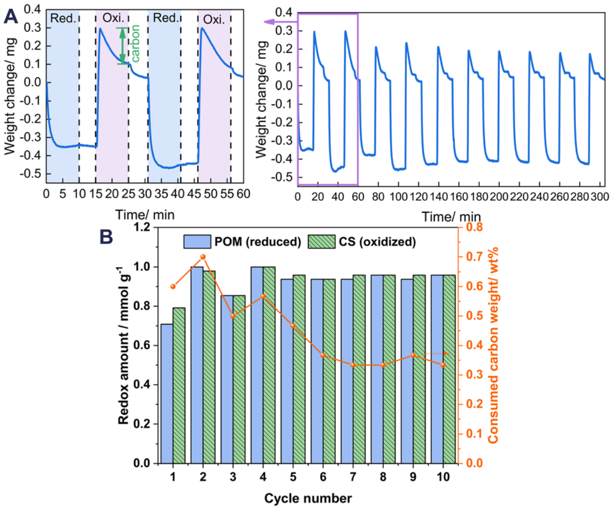

Fig. 4 (A) TGA of 1Ru/LCO during 10-cycle redox tests performed in alternating CH_4 and CO_2 flow. (B) Calculated data from the TGA profile.

Characterisations – structural and micromorphological evolution

Fig. 5A depicts the XRD patterns of the CeO_2, LCO, and 1Ru-promoted LCO samples: as-made, after reduction, after oxidation, and after 10 cycles. Only a simple pattern ascribed to the fluorite structure of CeO_2 was observed, with no extra diffraction phases. This lack of extra diffraction phases illustrates that the fluorite structure of CeO_2 is maintained after La substitution or Ru loading. The diffraction peaks of LCO shift towards lower degrees compared to those of CeO_2.

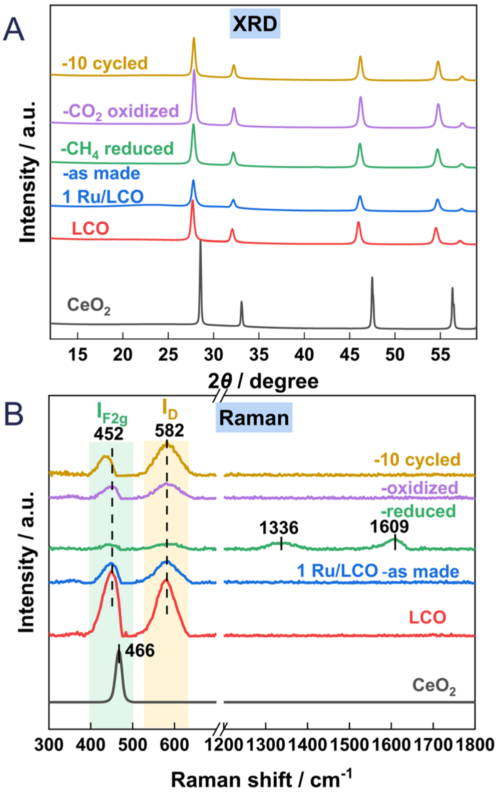

Fig. 5 (A) XRD patterns and (B) Raman profiles of CeO_2, LCO, 1Ru/LCO (as made, reduced, oxidised and 10 cycled) samples.

This shift results from the incorporation of La^{3+} into the lattice of CeO_2, leading to an increase in lattice parameters because of the augmented number of oxygen vacancies and the larger cation diameter of La^{3+}. The mean size of CeO_2 is markedly smaller after La doping. There is no observable peak ascribable to Ru in *x*Ru/LCO in Fig. S3,† indicating that Ru is highly dispersed and that no phase separation occurs within 5 wt% loading amounts. It is noteworthy that no readily apparent shift or observable peak ascribable to Ru is observed between the diffraction peaks of the reduced, oxidised, and 10-cycled 1Ru/LCO samples, indicating that the 1Ru/LCO retains structural stability with Ru highly dispersed during 10 successive DRM–CL redox cycles. Moreover, as Table 1 shows, the mean size of 1Ru/LCO remained stable without remarkable change after reduction, oxidation, or even 10 cycles. This stability might be related to the formation of strong Ru–O–Ce bonds at the $Ru^{\delta+}$–CeO_{2-x} interface, as confirmed by XPS results described hereinafter.

Raman spectroscopy was used to elucidate the oxygen vacancies formation in CeO_2 lattice. Fig. 5B shows Raman spectra of CeO_2, LCO, 1Ru/LCO, and 1Ru/LCO during/after DRM–CL cycle samples. Strong peaks at approx. 452 cm^{-1} attributed to the F_{2g} vibration mode of the Ce–O bond, are observed on all samples. Moreover, an additional peak at approx. 582 cm^{-1} attributed to defect-induced (D) modes of the fluorite phase[23,24] was observed for samples related to LCO, indicating that the doping of La induces the appearance of the subsurface oxygen vacancies. Moreover, the ratios of $I_D/I_{F_{2g}}$, indicating the relative concentrations of oxygen vacancies in CeO_2 lattice, are presented in Table 1. The higher $I_D/I_{F_{2g}}$ ratio in 1Ru/LCO compared to that in LCO indicates that the introduction of a small amount of Ru promoter enhances the formation of oxygen vacancies effectively. This enhancement is likely to be attributable to the formation of a strong Ru–O–Ce bond at the $Ru^{\delta+}$–CeO_{2-x} interface, as confirmed hereinafter based on XPS and *in situ* CO-DRIFTS results. The existing literature acknowledges that oxygen vacancies play a crucially important role in facilitating CH_4 activation by reducing the dissociation barriers of CH_3, CH_2, and CH radicals.[25]

Moreover, the $I_D/I_{F_{2g}}$ ratio of 1Ru/LCO greatly increases after reduction and decreases slightly after oxidation because the lattice oxygen was released in the reduction step and was refilled in the re-oxidation step. Two peaks at 1336 and 1609 cm^{-1} attributed to carbon species were observed after reduction, but they disappeared during re-oxidation,[26,27] indicating that carbon deposited during the reduction step can be consumed by CO_2 during the oxidation step. It is noteworthy that 1Ru/LCO shows a much higher the $I_D/I_{F_{2g}}$ ratio than after first oxidation after 10 cycles because more lattice oxygen is involved with reduction by CH_4 for 10 times.

The STEM, EDS element mappings, and high-resolution STEM results obtained for the fresh, reduced, and oxidised 1Ru/LCO are depicted in Fig. 6, whereas those for the 10 cycled 1Ru/LCO are presented in Fig. S4.† The STEM images revealed that the particle size of 1Ru/LCO remains consistent at 20–30 nm throughout the entire DRM–CL process, even after 10 cycles (consistent with mean size results calculated from XRD in Table 1), further confirming the structural stability of 1Ru/LCO. However, the CO pulse experiment revealed a mean diameter of Ru metal at 265.6 nm, which deviates considerably from results obtained using STEM and XRD. This disparity can be attributed to the formation of surface $Ru^{\delta+}$ resulting from SMSI effects between Ru and $La_2Ce_2O_7$. This formation decreases the amount of CO adsorption on the surface Ru metal and engenders inaccurate results for the Ru particle size. This observation indirectly underscores the presence of SMSI in the system. Moreover, high-resolution STEM images show that only two lattice fringes corresponding to (111) and (200) of CeO_2 are detected in the samples of fresh, reduced, oxidised, and 10 cycled 1Ru/LCO.[28,29] This single-phase of CeO_2 with the apparent absence of La and Ru particles suggests that La particles are well incorporated into the crystalline phase of CeO_2, whereas Ru components exist as highly dispersed RuO_x species over the LCO, aligning with XRD results. Of paramount

Table 1 Textual parameters of the LCO and 1Ru/LCO as made and during DRM–CL

Sample	S_{BET}[a] (m^2 g^{-1})	Mean size[b] (nm)	$I_D/I_{F_{2g}}$[c]
LCO		20.8	0.88
1Ru/LCO-as made	11.2	20.7	1.10
1Ru/LCO-reduced	13.2	19.2	1.37
1Ru/LCO-oxidised	11.5	22.4	1.31
1Ru/LCO-10 cycled	7.3	23.8	1.67

[a] Determined by the BET method. [b] Estimated by the Scherrer equation based on the reflection of CeO_2. [c] Calculated from the Raman results.

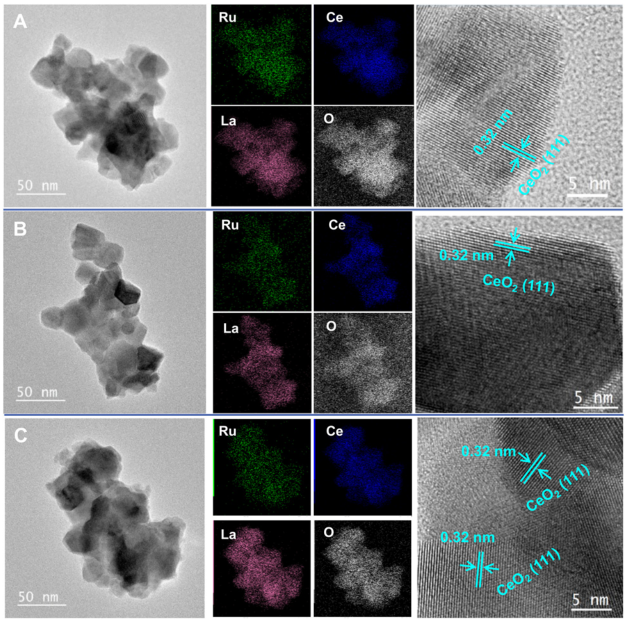

Fig. 6 STEM images, EDS element mappings and high-resolution STEM images of 1Ru/LCO (A) fresh, (B) CH_4 reduced, (C) CO_2 re-oxidised samples.

importance is that the results of EDS element mappings demonstrate that all elements, especially Ru, maintain high dispersion throughout the entire DRM–CL process, even after 10 cycles. No aggregation is observed, reflecting that Ru particles are anchored on the stable LCO support through the strong Ru–O–Ce bond at the $Ru^{\delta+}$–CeO_{2-x} interface, ensuring high stability.

Surface chemistry

As illustrated in Fig. 7A, the XPS Ce 3d spectra exhibit five pairs of $3d_{5/2}$ and $3d_{3/2}$ characteristic peaks. Three pairs, with peaks at 881.7, 887.9, and 897.2 eV, each accompanied by peaks at 900.1, 906.6, and 916.8 eV, are attributed to Ce^{4+} species, whereas the remaining two pairs are associated with Ce^{3+} species (some peaks with nearly zero area values appear as a result of fitting optimisation).[30,31] The Ce^{3+} ratio, calculated using the peak areas of $Ce^{3+}/(Ce^{3+} + Ce^{4+})$, is an important indicator of the oxygen vacancies on ceria surfaces.[32,33] It is noteworthy that the Ce^{3+} ratio of the samples after CH_4 reduction at 923 K is markedly lower than that of the fresh sample, pretreated with H_2 at 673 K for 30 min. This finding is likely attributable to the heating process from 673 K to 923 K, which accelerates the diffusion of oxide ions inside the oxygen carrier material. Consequently, the oxygen vacancies become more homogeneously distributed in the surface and subsurface layers, potentially resulting in a relative reduction in the surface Ce^{3+} ratio. Moreover, the Ce^{3+} ratio increases consistently from 9.6% to 13.3% with CH_4 reduction from 2 min to 10 min, indicating augmentation in oxygen vacancies on ceria surfaces resulting from the POM reaction through the reduction of Ce^{4+} to Ce^{3+}. Subsequently, the Ce^{3+} ratio decreases markedly to 3.6% after 10 min of CO_2 reoxidation, indicating the efficient refilling of surface oxygen vacancies through the oxidation of Ce^{3+} to Ce^{4+}.

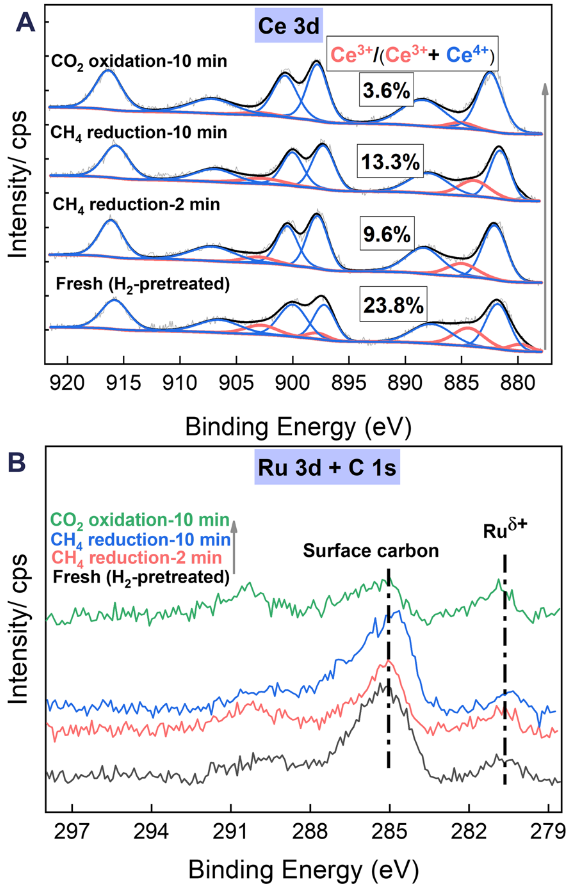

Fig. 7 The XPS data for the (A) Ce 3d and (B) C 1s + Ru 3d regions of the 1Ru/LCO sample after undergoing a series of sequential pretreatments: H_2 pretreatment at 673 K for 30 min, CH_4 reduction at 923 K for 2 and 10 min, and CO_2 reoxidation at 923 K for 10 min.

In the XPS spectra of C 1s + Ru 3d (Fig. 7B), the Ru 3d5/2 is commonly used to understand the charge state of Ru species because of the overlapping of Ru $3d_{3/2}$ and C 1s peak at approximately the 284.8 eV position. Throughout the entire redox process, peaks attributed to partially charged Ru nano particles ($Ru^{\delta+}$) at around 280.8 eV position are observed. This phenomenon is associated with charge transfer during the formation of the Ru–O–Ce species, contributing to the enhancement of oxygen vacancies. Similar observations have been reported widely for other ceria-supported Ru systems. Liu *et al.*[10] reported that the Ru nanoparticles supported on ceria with $Ru^{\delta+}$ and O decoration exhibit much better stability than those with only metallic Ru^0 under steady-state DRM conditions because of their sustained active chemistry. Furthermore, earlier theoretical investigations into the activation of methane over CeO_2-supported transition metals suggested that strong interaction between the metal and ceria support and acquisition of positive charges constitute markedly lower methane activation barriers.[25,34,35]

Simultaneously, the spectra and quantitative results presented in Table 2 reveal continuous accumulation of surface carbon (approx. 284.9 eV) attributable to methane decomposition during the reduction by CH_4 from 2 to 10 min. This carbon accumulation decreases considerably to levels lower than those after 2 min of CH_4 reduction following 10 min of CO_2 reoxidation. This decrease further confirms the consumption of deposited carbon during CO_2 reoxidation, which is consistent with results obtained from Raman and TGA analyses.

To gain additional insights into the surface adsorption condition changes occurring during the DRM–CL process of 1Ru/LCO, *in situ* CO-adsorption DRIFTS was performed for the fresh, reduced, and oxidised 1Ru/LCO. The results are presented in Fig. 8. Upon the fresh 1Ru/LCO surface in Fig. 8A, IR bands at 2176 and 2116 cm^{-1}, attributed to

Table 2 Quantitative results of XPS for the 1Ru/LCO sample after undergoing a series of sequential pretreatments

Sample	Ce	La	O/atom%	C	Ru
H_2 treatment	9.7	13.0	53.7	23.4	0.2
CH_4 2 min	10.5	14.0	57.2	18.1	0.2
CH_4 10 min	9.8	12.8	53.8	23.5	0.1
CO_2 10 min	10.8	14.8	61.3	12.9	0.2

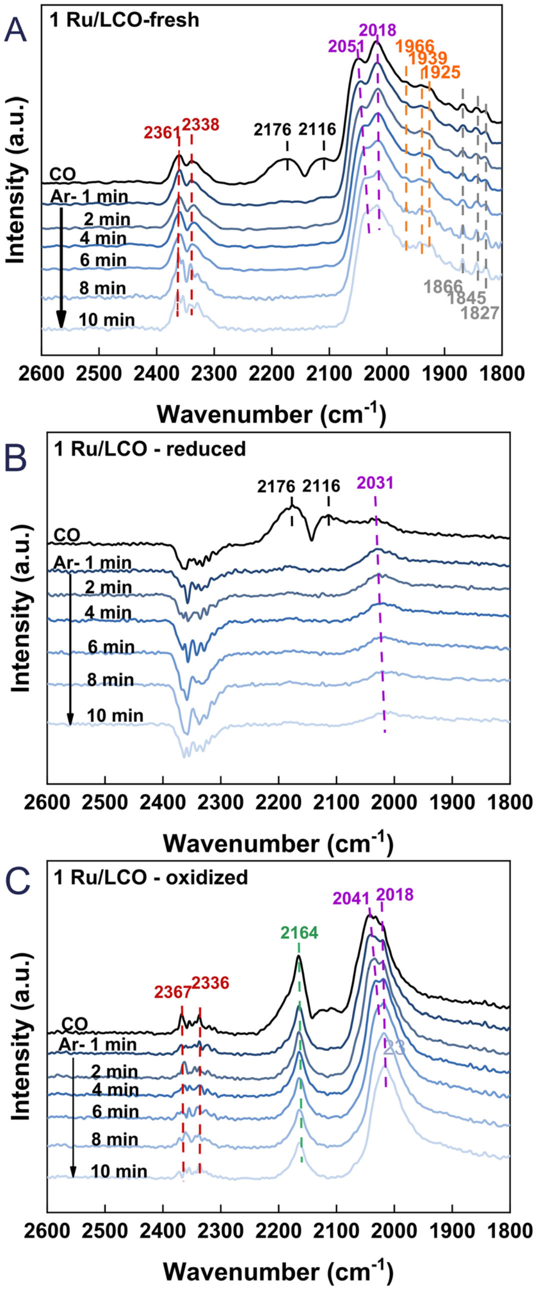

Fig. 8 *In situ* CO-DRIFTS of 1Ru/LCO (A) fresh (B) reduced by CH_4 and (C) oxidized by CO_2.

gaseous CO, disappear rapidly after 1 min Ar purging. Additionally, bands at 1866, 1845, and 1827 cm^{-1} correlated with bridge-bound CO adsorption on Ru atoms are observed along with two prominent bands at 2051 and 2018 cm^{-1} assigned to linearly absorbed CO on Ru atoms,[36–38] showing that Ru species are well-dispersed on the surface. It is noteworthy that bands are visible at 1966, 1939, and 1925 cm^{-1}, corresponding to CO adsorption on the interface of the Ru metal and LCO support.[39,40] These further validate the XPS results, indicating interactions between the LCO support and Ru clusters. On the reduced 1Ru/LCO surface in Fig. 8B, except for the quickly disappearing bands attributed to gaseous CO, only one band associated with absorbed CO on Ru atoms remains, resulting from the surface partially covered by carbon deposited from CH_4 decomposition. On the oxidised sample surface in Fig. 8C, bands related to Ru metal atoms reappear, suggesting that CO_2 reoxidation removes deposited carbon effectively, thereby uncovering the surface and regenerating the adsorption sites of the material for the next cycle. Additionally, a distinctive band is apparent at 2164 cm^{-1}, attributed to CO adsorbed onto Ce^{4+} cations with different unsaturated coordination.[41–43] That band constitutes evidence for the completion of oxygen vacancy refilling and oxygen migration from the subsurface to the surface during the transition from Ce^{3+} to Ce^{4+}. Importantly, IR bands at 2361 and 2338 cm^{-1} positions, attributed to linearly or physically adsorbed CO_2,[26,44] resulting from the reaction between CO adsorbed onto surface oxygen vacancies and oxygen species, were observed on both fresh and oxidised sample surfaces. Those bands reflect an abundance of surface oxygen vacancies for CH_4 activation, related to the strong interaction through the formation of Ru–O–Ce. This interaction endures even after cycling, demonstrating the remarkable stability of 1Ru/LCO.

Discussion

Based on analyses of structural and electronic properties, the proposed reaction processes of DRM–CL over 1Ru/LCO oxygen carrier are presented in Fig. 9. Specifically, in the reduction step, the activated CH_4 releases the lattice oxygen through the transition from Ce^{4+} to Ce^{3+}, with the formation of oxygen vacancies. Then in the oxidation step, CO_2 is adsorbed and dissociated on the surface of 1Ru/LCO oxygen carrier with progress of the oxidation step, thereby re-filling the oxygen vacancies. This sequence is repeated iteratively, completing each redox cycle. The presence of surface $Ru^{\delta+}$ plays a crucially important role in enhancing the performance of both the oxidation and reduction steps and contributing to the overall cyclic stability.

The CH_4-TPR and redox performance presented in Fig. 2 and 3 demonstrate the remarkable efficiency of a small amount of 0.5 or 1 wt% Ru promoter for enhancing the CH_4 activation ability of LCO. This enhancement leads to a low CH_4 activation onset temperature of approximately 545 K, achieving approximately 65% CH_4 conversion, even at 723 K. Raman (Fig. 5B), XPS (Fig. 7), and *in situ* CO-adsorption

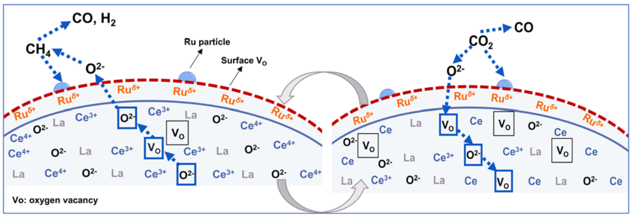

Fig. 9 Proposed reaction processes of DRM–CL over 1Ru/LCO oxygen carrier.

DRIFTS (Fig. 8) results emphasise the fundamentally important role played by oxygen vacancies and the Ru–O–Ce bond formed because of SMSI in supporting the superior CH_4 reactivity. The formation of Ru–O–Ce bonds at the RuO_x–CeO_{2-x} interface, as supported by density functional theory calculations[45] and experiments,[46] decreases the oxygen vacancy formation energy, consequently improving low-temperature CH_4 reactivity. Moreover, the well-dispersed $Ru^{\delta+}$ species in the form of Ru–O–Ce bonds contribute to mobile and active oxygen ions for DRM–CL processes.

The performance results presented in Fig. 3 also show CO_2 conversion greater than 95% at 723 K in the CO_2 reoxidation step. Earlier studies of surface-promoted oxygen carriers highlight the importance of the potential gradient between the oxide bulk (or subsurface) and surface induced by the prompted surface for O^{2-} migration.[8] In our case, the oxygen-deprived surface in the presence of Ru establishes an increased oxygen chemical potential gradient between the oxide subsurface and surface. This enhancement engenders improved O^{2-} migration, facilitated by the redox reaction between Ce^{3+} and Ce^{4+} in the subsurface of the oxygen carrier, ultimately completing the chemical looping process and promoting CO_2 conversion.

Cycle stability tests for the gas phase demonstrate excellent redox performance over 10 cycles (Fig. 3C and 4A), with observation of the removal of the deposited carbon in the reoxidation step by TGA (Fig. 4), Raman (Fig. 5B and Table 1), and XPS (Fig. 6 and Table 2). Additionally, XRD (Fig. 6A), BET (Table 1), and STEM-EDS (Fig. 6) findings demonstrate that the structure of 1Ru/LCO remains stable after 10 cycles, with Ru maintaining a highly dispersed state. This state is attributed to the formation of Ru–O–Ce bonds anchoring active Ru onto stable $La_2Ce_2O_7$ with excellent ionic conductivity, highlighting its strong anti-aggregation capability.

Conclusions

$Ru/La_2Ce_2O_7$ catalytic chemical looping material is highly effective for enhancing CH_4 activation even at low temperatures (545 K). The 1 wt% Ru/LCO demonstrates remarkable performance, achieving CH_4 conversion of approximately 65%, with minimal CO_2 production during the reduction step and CO_2 conversion exceeding 95% during the CO_2 re-oxidation step at 923 K over 10 redox cycles. Despite encountering slight carbon deposition during the reduction step, the redox performance maintains stability in 10 successive cycles because of the efficient carbon conversion which occurs during the reoxidation step and because of the inherent structure stability of the oxygen carrier. This exceptional performance is attributed to the establishment of a strong metal–support interaction between Ru and $La_2Ce_2O_7$, forming crucially important Ru–O–Ce bonds. These bonds anchor the active Ru species onto the stable and ionic conductive $La_2Ce_2O_7$ substrate. This mechanism enhances CH_4 activation by increasing surface oxygen vacancies. Moreover, it maintains structural stability with well-dispersed Ru promoters throughout the cyclic process. Furthermore, the oxygen-deprived surface induced by Ru presence creates an elevated oxygen chemical potential gradient between the oxide subsurface and surface, improving O^{2-} migration for the redox reaction between Ce^{3+} and Ce^{4+} in the subsurface of the oxygen carrier to accomplish the chemical looping process effectively.

Author contributions

Conceptualisation: KK and YS, funding acquisition: YS, investigation: KK, NK, CS, project administration: YS, supervision: YS, validation: KK, NK, TH, CS, YS, visualization: KK, writing – original draft: KK, writing – review & editing: YS.

Conflicts of interest

There are no conflicts to declare.

Acknowledgements

Equipment (JEM-2100F: Material Characterization Central Laboratory in Waseda University) shared with the MEXT Project for Promoting Public Utilization of Advanced Research Infrastructure (Program for supporting the construction of core facilities) under grant numbers JPMXS0440500022, and JPMXS0440500023 was used. A part of this work was supported by JST-ALCA-Next Program Grant Number 23836167, Japan, and International Leading Research (grant no. 23K20034) from the Japan Society for the Promotion of Science, Japan. The author acknowledges the financial support from the China Scholarship Council (Grant No. 202104910057).

References

1 N. A. K. Aramouni, J. G. Touma, B. A. Tarboush, J. Zeaiter and M. N. Ahmad, *Renewable Sustainable Energy Rev.*, 2018, **82**, 2570–2585.

2 M. Usman, W. M. A. Wan Daud and H. F. Abbas, *Renewable Sustainable Energy Rev.*, 2015, **45**, 710–744.

3 J. Wei and E. Iglesia, *Angew. Chem., Int. Ed.*, 2004, **43**, 3685–3688.

4 Q. Zhang, W. Deng and Y. Wang, *J. Energy Chem.*, 2013, **22**, 27–38.

5 A. Shafiefarhood, N. Galinsky, Y. Huang, Y. G. Chen and F. X. Li, *ChemCatChem*, 2014, **6**, 790–799.

6 A. Shafiefarhood, J. C. Hamill, L. M. Neal and F. Li, *Phys. Chem. Chem. Phys.*, 2015, **17**, 31297–31307.

7 L. M. Neal, A. Shafiefarhood and F. Li, *ACS Catal.*, 2014, **4**, 3560–3569.

8 A. Shafiefarhood, J. Zhang, L. M. Neal and F. Li, *J. Mater. Chem. A*, 2017, **5**, 11930–11939.

9 Z. Liu, D. C. Grinter, P. G. Lustemberg, T.-D. Nguyen-Phan, Y. Zhou, S. Luo, I. Waluyo, E. J. Crumlin, D. J. Stacchiola, J. Zhou, J. Carrasco, H. F. Busnengo, M. V. Ganduglia-

Pirovano, S. D. Senanayake and J. A. Rodriguez, *Angew. Chem., Int. Ed.*, 2016, **55**, 7455–7459.

10 Z. Liu, F. Zhang, N. Rui, X. Li, L. Lin, L. E. Betancourt, D. Su, W. Xu, J. Cen, K. Attenkofer, H. Idriss, J. A. Rodriguez and S. D. Senanayake, *ACS Catal.*, 2019, **9**, 3349–3359.

11 S. Miyazaki, Z. Li, Z. Maeno, T. Toyao, M. Ito, Y. Nakajima and K.-I. Shimizu, *Chem. Lett.*, 2022, **51**, 914–918.

12 K. Otsuka, Y. Wang, E. Sunada and I. Yamanaka, *J. Catal.*, 1998, **175**, 152–160.

13 S. Assabumrungrat, S. Charoenseri, N. Laosiripojana, W. Kiatkittipong and P. Praserthdam, *Int. J. Hydrogen Energy*, 2009, **34**, 6211–6220.

14 K. Otsuka, Y. Wang, E. Sunada and I. Yamanaka, *J. Catal.*, 1998, **175**, 152–160.

15 F. R. García-García and I. S. Metcalfe, *Catal. Commun.*, 2021, **160**, 106356.

16 J. Guerrero-Caballero, T. Kane, N. Haidar, L. Jalowiecki-Duhamel and A. Löfberg, *Catal. Today*, 2019, **333**, 251–258.

17 M. Tang, K. Liu, D. M. Roddick and M. Fan, *J. Catal.*, 2018, **368**, 38–52.

18 B. Choudhary, L. Besra, S. Anwar and S. Anwar, *Int. J. Hydrogen Energy*, 2023, **48**, 28460–28501.

19 Q. Zhang, X. Zheng, J. Jiang and W. Liu, *J. Phys. Chem. C*, 2013, **117**, 20379–20386.

20 A. P. Ramon, X. Li, A. H. Clark, O. V. Safonova, F. C. Marcos, E. M. Assaf, J. A. van Bokhoven, L. Artiglia and J. M. Assaf, *Appl. Catal., B*, 2022, **315**, 121528.

21 P. Ferreira-Aparicio, C. Márquez-Alvarez, I. Rodríguez-Ramos, Y. Schuurman, A. Guerrero-Ruiz and C. Mirodatos, *J. Catal.*, 1999, **184**, 202–212.

22 A. J. Carrillo, L. Navarrete, M. Laqdiem, M. Balaguer and J. M. Serra, *Adv. Mater.*, 2021, **2**, 2924–2934.

23 Z. Xu, H. Tian, A. Khanaki, R. Zheng, M. Suja and J. Liu, *Sci. Rep.*, 2017, **7**, 43100.

24 C. Zheng, D. Mao, Z. Xu and S. Zheng, *J. Catal.*, 2022, **411**, 122–134.

25 Z. Cheng, L. Qin, M. Guo, J. A. Fan, D. Xu and L.-S. Fan, *Phys. Chem. Chem. Phys.*, 2016, **18**, 16423–16435.

26 Z. Cao, X. Zhu, K. Li, Y. Wei, F. He and H. Wang, *Chem. Eng. J.*, 2020, **397**, 125393.

27 Y. Han, M. Tian, C. Wang, Y. Kang, L. Kang, Y. Su, C. Huang, T. Zong, J. Lin, B. Hou, X. Pan and X. Wang, *ACS Sustainable Chem. Eng.*, 2021, **9**, 17276–17288.

28 K. Kang, X. Yao, J. Cao, Z. Li, J. Rong, W. Luo, W. Zhao and Y. Chen, *J. Hazard. Mater.*, 2021, **402**, 123551.

29 Z. Zhang, Y. Wang, M. Wang, J. Lü, L. Li, Z. Zhang, M. Li, J. Jiang and F. Wang, *Chin. J. Catal.*, 2015, **36**, 1623–1630.

30 M. Romeo, K. Bak, J. El Fallah, F. Le Normand and L. Hilaire, *Surf. Interfaces*, 1993, **20**, 508–512.

31 B. Lin, Y. Liu, L. Heng, X. Wang, J. Ni, J. Lin and L. Jiang, *Ind. Eng. Chem. Res.*, 2018, **57**, 9127–9135.

32 H. Huang, Q. Dai and X. Wang, *Appl. Catal., B*, 2014, **158–159**, 96–105.

33 N. Wang, W. Qian, W. Chu and F. Wei, *Catal. Sci. Technol.*, 2016, **6**, 3594–3605.

34 Z. Liu, P. Lustemberg, R. A. Gutiérrez, J. J. Carey, R. M. Palomino, M. Vorokhta, D. C. Grinter, P. J. Ramírez, V. Matolín, M. Nolan, M. V. Ganduglia-Pirovano, S. D. Senanayake and J. A. Rodriguez, *Angew. Chem., Int. Ed.*, 2017, **56**, 13041–13046.

35 P. G. Lustemberg, P. J. Ramírez, Z. Liu, R. A. Gutiérrez, D. G. Grinter, J. Carrasco, S. D. Senanayake, J. A. Rodriguez and M. V. Ganduglia-Pirovano, *ACS Catal.*, 2016, **6**, 8184–8191.

36 D. Yubero Valdivielso, C. Kerpal, W. Schöllkopf, G. Meijer and A. Fielicke, *Dalton Trans.*, 2023, **52**, 9929–9939.

37 J. Li, Z. Liu, D. A. Cullen, W. Hu, J. Huang, L. Yao, Z. Peng, P. Liao and R. Wang, *ACS Catal.*, 2019, **9**, 11088–11103.

38 G. H. Yokomizo, C. Louis and A. T. Bell, *J. Catal.*, 1989, **120**, 1–14.

39 O. Pozdnyakova, D. Teschner, A. Wootsch, J. Kröhnert, B. Steinhauer, H. Sauer, L. Toth, F. C. Jentoft, A. Knop-Gericke, Z. Paál and R. Schlögl, *J. Catal.*, 2006, **237**, 1–16.

40 P. Bazin, O. Saur, J. C. Lavalley, M. Daturi and G. Blanchard, *Phys. Chem. Chem. Phys.*, 2005, **7**, 187–194.

41 C. Binet, M. Daturi and J.-C. Lavalley, *Catal. Today*, 1999, **50**, 207–225.

42 A. Badri, C. Binet and J.-C. Lavalley, *J. Chem. Soc., Faraday Trans.*, 1996, **92**, 4669–4673.

43 M. I. Zaki, B. Vielhaber and H. Knoezinger, *J. Phys. Chem.*, 1986, **90**, 3176–3183.

44 G. Deng, G. Zhang, X. Zhu, Q. Guo, X. Liao, X. Chen and K. Li, *Appl. Catal., B*, 2021, **289**, 120033.

45 H.-T. Chen, *J. Phys. Chem. C*, 2012, **116**, 6239–6246.

46 M. Kurnatowska, W. Mista, P. Mazur and L. Kepinski, *Appl. Catal., B*, 2014, **148–149**, 123–135.